Nano Research

Open Access

Research Article

Pseudohalide engineering for crystallization kinetics and defect passivation in two-step fabricated $Cs_{0.1}FA_{0.9}Pb_{0.9}Sn_{0.1}I_3$ perovskite solar cells with exceptional efficiency and stability

Lina Qin[1,§], Mengfei Zhu[1,§], Yuren Xia[1], Daocheng Hong[1], Yuxi Tian[1], Huapeng Sun[4] ✉, Zuoxiu Tie[1,2,3] ✉, Yan Xiong[1] ✉, and Zhong Jin[1,2,3] ✉

[1] *State Key Laboratory of Coordination Chemistry, MOE Key Laboratory of Mesoscopic Chemistry, MOE Key Laboratory of High Performance Polymer Materials and Technology, Jiangsu Key Laboratory of Advanced Organic Materials, Suzhou Key Laboratory of Green Intelligent Manufacturing of New Energy Materials and Devices, Tianchang New Materials and Energy Technology Research Center, Institute of Green Chemistry and Engineering, School of Chemistry and Chemical Engineering, Nanjing University, Nanjing 210023, China*
[2] *Nanjing Tieming Energy Technology Co. Ltd., Nanjing 210093, China*
[3] *Suzhou Tierui New Energy Technology Co. Ltd., Suzhou 215228, China*
[4] *School of New Energy, Chenjiang Laboratory, Chenzhou Vocational Technical College, Chenzhou 423000, China*
[§] *Lina Qin and Mengfei Zhu contributed equally to this work.*

Cite this article: *Nano Research*, **2025**, *18*, 94907845. https://doi.org/10.26599/NR.2025.94907845

ABSTRACT: Organic-inorganic hybrid perovskite solar cells (PSCs) have emerged as a leading photovoltaic technology due to their exceptional power conversion efficiency (PCE) and low-cost fabrication process. However, the intrinsic thermal instability of organic cations, such as methylammonium (MA^+) and formamidinium (FA^+), necessitates their partial or complete substitution with inorganic cesium (Cs^+) ions to enhance thermal robustness. While all-inorganic $CsPbI_3$ exhibits superior thermal stability, its susceptibility to moisture and phase instability limits its practical applicability. Moreover, the toxicity of lead (Pb) has driven interest in tin (Sn) as a more sustainable alternative. In this study, we investigate the incorporation of pseudo-halide thiocyanate anions (SCN^-) as a crystallization modulator for two-step spin-coating preparation of $Cs_{0.1}FA_{0.9}Pb_{0.9}Sn_{0.1}I_3$ film, which promotes the formation of lead iodide coordination intermediates and lowering the energy barrier for perovskite crystal growth. By integrating Cs^+ and Sn^{2+} into $FAPbI_3$ perovskites with SCN^- additives, the compositions, crystallinity, and grain interfaces of $Cs_{0.1}FA_{0.9}Pb_{0.9}Sn_{0.1}I_3$ film are well tuned, yielding a PCE of 21.34%. The resulting PSCs demonstrated superior long-term stability and enhanced thermal resistance, highlighting the immense potential of SCN^- mediated crystallization and tailored compositional engineering as effective strategies for the development of high-performance and thermally endurable PSCs.

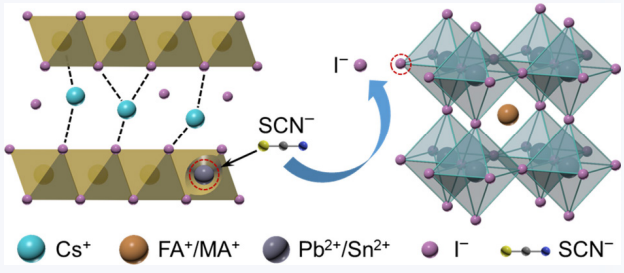

KEYWORDS: perovskite solar cells, thermal stability, pseudo-halide thiocyanate (SCN^-) modulation, tin doping, crystallization control

1 Introduction

Organic-inorganic hybrid perovskite solar cells (PSCs) have emerged as a prominent technology due to their high power conversion efficiency (PCE) and low fabrication costs. Early studies predominantly focused on perovskites featuring organic A-site cations such as methylammonium (MA^+) and formamidinium (FA^+), which, despite their promising optoelectronic properties, were hindered by inadequate thermal stability [1–3]. To mitigate this limitation, the substitution of organic cations with inorganic cesium (Cs^+) ions has been investigated, demonstrating improved thermal robustness [4, 5]. Fully inorganic perovskites, such as $CsPbI_3$, exhibit exceptional thermal stability but remain stable exclusively at elevated temperatures, undergoing a reversible phase transition from a yellow orthorhombic phase to a dark cubic phase

Received: May 18, 2025; **Revised:** July 17, 2025
Accepted: July 24, 2025

✉Address correspondence to Huapeng Sun, huapengsun@hotmail.com; Zuoxiu Tie, zxtie@nju.edu.cn; Yan Xiong, xiongyan@nju.edu.cn; Zhong Jin, zhongjin@nju.edu.cn

at 308 °C. Additionally, the pronounced moisture sensitivity of $CsPbI_3$ limits its practical application in photovoltaic devices [6]. The introduction of a solid solution between $FAPbI_3$ and $CsPbI_3$ at ambient temperature has enabled the partial incorporation of Cs^+ into $FAPbI_3$, thereby reducing the formation energy of the cubic phase. This modification enhances the structural stability and facilitates more favorable reaction conditions, partially addressing key challenges associated with the performance and scalability of PSCs [7].

On the other hand, lead (Pb) is extensively used in perovskite materials. However, its significant environmental and health hazards necessitate the development of alternative solutions. Tin (Sn), as a group IV element with chemical properties and an ionic radius similar to Pb, making it a promising substitute due to its higher natural abundance [8]. Liang et al. successfully incorporated Sn into fully inorganic $CsPbI_2Br$ perovskites via a two-step method, achieving an optimal bandgap of 1.79 eV along with enhanced thermal and moisture stability [9]. Recent studies by Satyaprasad et al. demonstrated that Sn doping effectively reduces ion migration, supported by electronic structure calculations and biased photoluminescence. Additionally, Pb/Sn mixed perovskites exhibit enhanced environmental stability compared to pure Sn-based perovskites [10]. Pseudo-halide ion (SCN^-), commonly incorporated in perovskite precursor solutions or employed as a post-treatment additive via a one-step spin-coating process, offers controllable coordination and dissociation with Pb^{2+} ions [11–13]. To achieve a PCE exceeding 23%, researchers frequently employ a two-step spin-coating method, which enables precise crystallization control [14]. However, the elevated energy state of this method may lead to incomplete reactions, requiring the use of additives to optimal crystallinity. The incorporation of SCN^- as a crystallization aid offers a viable approach to enhancing the efficiency and reliability of the two-step spin-coating process.

Herein, we report the use of organic salts containing pseudo-halide thiocyanate (SCN^-) as additives to enhance the formation of coordination intermediates with lead iodide, thereby reducing the energy barrier for perovskite crystal growth. Employing a two-step spin-coating technique, four perovskite films: $MAPbI_3$, $FAPbI_3$, $Cs_{0.1}FA_{0.9}PbI_3$, and $Cs_{0.1}FA_{0.9}Pb_{0.9}Sn_{0.1}I_3$ were fabricated. During the annealing process, SCN^- ions react with protons to generate HSCN gas, facilitating the volatilization of organic cations while preserving the integrity of the perovskite core structure. The incorporation of Cs^+ and Sn^{2+} dopants further improved the structural properties of the films, enabling the $Cs_{0.1}FA_{0.9}Pb_{0.9}Sn_{0.1}I_3$-based PSCs to achieve a power conversion efficiency of 21.343% and also exhibit outstanding long-term operational and thermal stability. This work offers a promising approach for high efficiency and thermally resistant PSCs through the synergy of pseudo-halide SCN^- ions and compositional engineering strategies.

2 Results and discussion

We employed a two-step spin-coating method employing MASCN or FASCN with pseudo-halide SCN^- as a secondary crystallization additive to fabricate four types of perovskite films: $MAPbI_3$, $FAPbI_3$, $Cs_{0.1}FA_{0.9}PbI_3$, and $Cs_{0.1}FA_{0.9}Pb_{0.9}Sn_{0.1}I_3$. Additionally, n–i–p structured PSCs were prepared with the ITO/SnO_2/perovskite/Spiro-OMeTAD/Au architecture. Comprehensive characterization analyses of these films and devices were conducted to evaluate their structural, optical, and electrical properties. Figure 1(a) presents a schematic model for SCN^--assisted crystallization mechanism of $Cs_{0.1}FA_{0.9}Pb_{0.9}Sn_{0.1}I_3$. Initially, SCN^- coordinates with PbI_2 via lone pair electrons on its sulfur atom, forming a PbI_2·SCN^- intermediate. This coordination stabilizes the PbI_2 layers and generates active sites for the infiltration of formamidinium iodide (FAI). During the spin-coating process, FAI interacts with the PbI_2·SCN^- intermediate, while SCN^- localizes at grain boundaries. Upon annealing, SCN^- reacts with protons to produce HSCN gas, which volatilizes, leading to the final perovskite phase. The incorporation of Cs^+ during spin-coating facilitates the integration of SCN^- by creating ionic channels, thereby promoting complete perovskite formation. Moreover, Sn^{2+} doping improves the surface smoothness and reduces the perovskite bandgap [15].

Figure 1(b) illustrates the color changes during film preparation. The step 1 involves precursor deposition without SCN^-, followed by Step 2 where the addition of SCN^- modulates perovskite nucleation at the wet film state prior to annealing. The perovskite film containing SCN^- exhibit a red coloration after the second spin-coating step, indicating the formation of PbI_2·SCN^- intermediate. After annealing, the SCN^--containing film appears glossy black, while the film without SCN^- remains blackish yellow and translucent. This contrast highlights the critical role of SCN^- as a pseudo-halide additive in the crystallization process. As shown in Fig. 1(c), X-ray diffraction (XRD) analysis was conducted to investigate the impact of SCN^- additives on the crystallinity of perovskite films prepared with four different compositions and various additive concentrations. The XRD peaks at 14.0° and 28.1° correspond to the (110) and (220) planes of cubic perovskite phase, respectively, while the peak at 12.6° indicates residual PbI_2. Additionally, some films exhibit a diffraction peak near 24.4°, corresponding to the (202) plane [7]. $MAPbI_3$ film lack a prominent PbI_2 peak, like due to the small ionic radius of MA^+ (217 pm), which lowers the formation energy of perovskite crystal [16]. In contrast, the $FAPbI_3$ film displays a pronounced PbI_2 peak, due to the larger ionic radius of FA^+ (253 pm), which hampers the incorporation of FAI into PbI_2·SCN^- intermediate [17]. The introduction of Cs^+ ions creates ionic channels for the second organic reactant, leading to a marked reduction in the intensity of PbI_2 peak. Furthermore, Sn^{2+} doping significantly diminishes the intensity of the (202) peak, indicating preferential crystal growth along the (110) and (220) planes. To further evaluate the influence of SCN^- concentration on perovskite crystallization, XRD analysis was performed on $Cs_{0.1}FA_{0.9}Pb_{0.9}Sn_{0.1}I_3$ films with various FASCN concentrations of 0, 20, 40, 60, and 80 mg/mL, respectively (Fig. 1(d)). At the concentrations between 0–60 mg/mL, the PbI_2 peak intensity decreases with increasing additive concentration, demonstrating the effective role of SCN^- in enhancing crystallization. However, at a concentration of 80 mg/mL, excessive FASCN incorporation leads to the formation of a $FA_2Pb(SCN)_6$ two-dimensional (2D) perovskite phase, as indicated by a low-angle peak at 11.8°, along with residual PbI_2. This observation underscores that excessively high SCN^- concentrations hinder the formation of α-perovskite cubic phase. Unlike traditional 2D perovskites employing large organic cation spacers (e.g., BA^+, PEA^+) that substantially increase interlayer d-spacing and shift XRD peaks to low angles (< 10°) according to Bragg's equation ($2d\sin\theta = n\lambda$), the smaller pseudohalide SCN^- spacer in this work reduces d-spacing. Consequently, a shift of the low-angle diffraction peak to higher angles, as its observation at 11.8° [18]. Figure 1(e) presents Raman spectroscopy results for PbI_2 films coated with FASCN. The

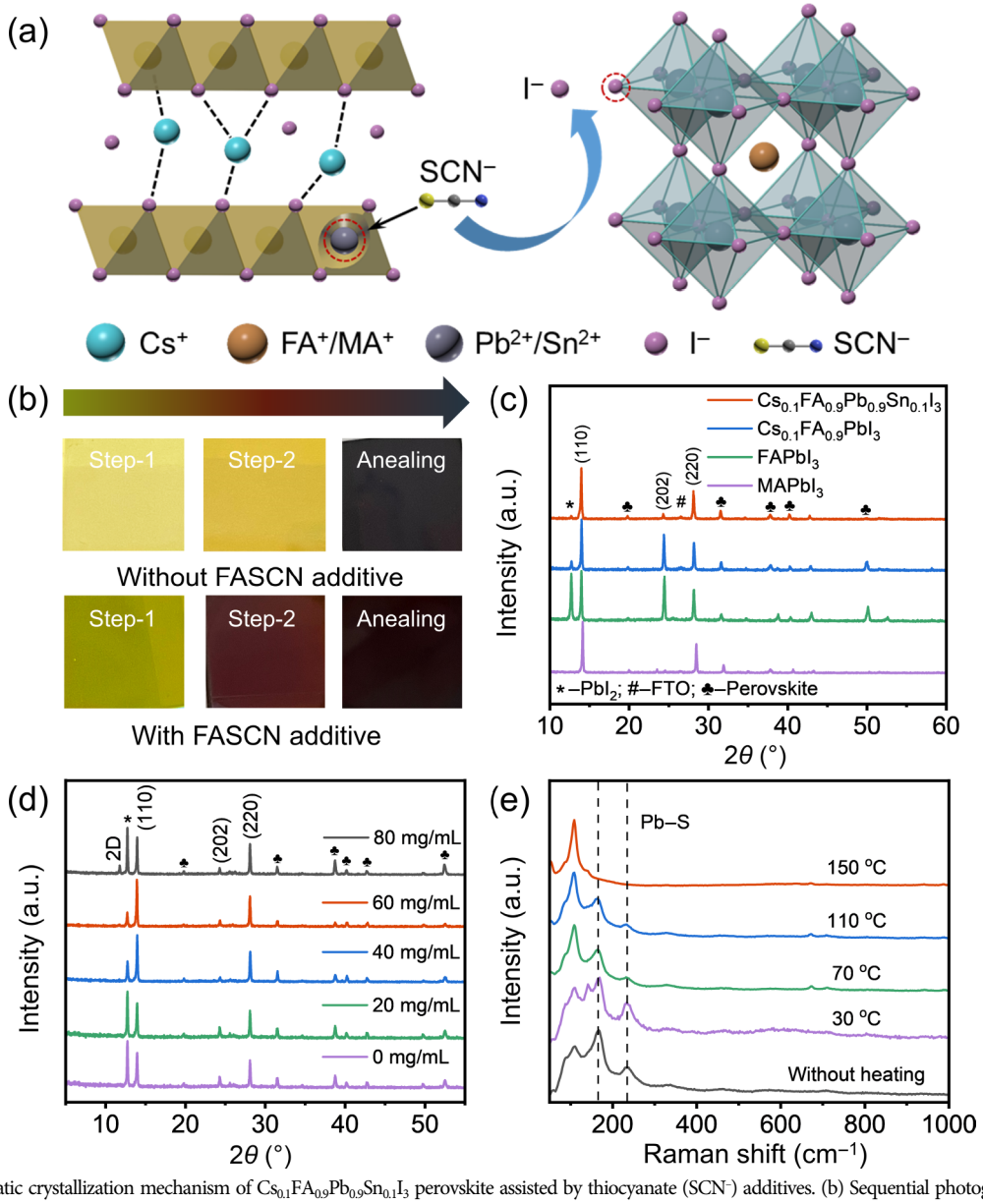

Figure 1 (a) Schematic crystallization mechanism of $Cs_{0.1}FA_{0.9}Pb_{0.9}Sn_{0.1}I_3$ perovskite assisted by thiocyanate (SCN^-) additives. (b) Sequential photographs illustrating the evolution of perovskite films with or without FASCN additive during the formation process. (c) XRD patterns of four types of as-prepared perovskite films: $MAPbI_3$, $FAPbI_3$, $Cs_{0.1}FA_{0.9}PbI_3$, and $Cs_{0.1}FA_{0.9}Pb_{0.9}Sn_{0.1}I_3$. (d) XRD patterns of $Cs_{0.1}FA_{0.9}Pb_{0.9}Sn_{0.1}I_3$ films prepared with different concentrations of SCN^- additives. (e) Raman spectra of the PbI_2·SCN intermediate without heating and heated at 30, 70, 110, and 150 °C, respectively.

peak at ~ 100 cm^{-1} is primarily attributed to Pb–I bond vibration, influenced by Sn^{2+} doping and SCN^- coordination that weakens Pb–I covalency [19]. Prior to annealing, characteristic peaks corresponding to Pb-S bond stretching vibrations are observed, confirming the binding of SCN^- to Pb^{2+} via sulfur lone pair electrons [20]. As the temperature rises, these peaks gradually diminish and vanish entirely at 150 °C. Both XPS (Fig. S1(d) in the ESM) and Raman analyses (Fig. 1(e)) confirm its volatilization of SCN^- during annealing. Since the SCN^- anion remains structurally stable at this temperature, its volatilization leaves no stable residues but enhances film quality and device performance through crystallization regulation and defect passivation.

The microstructural morphologies of $Cs_{0.1}FA_{0.9}Pb_{0.9}Sn_{0.1}I_3$, $Cs_{0.1}FA_{0.9}PbI_3$, $FAPbI_3$ and $MAPbI_3$ perovskite films were analyzed using scanning electron microscopy (SEM), as illustrated in Figs. 2(a)–2(d). The SEM images reveal that $MAPbI_3$ perovskite exhibits the smallest grain size with a pervasive distribution of pinholes, leading to poor film uniformity. In contrast, $FAPbI_3$ perovskite shows slightly larger grains, albeit with distorted crystal shapes and a persistence of pinholes. These morphological defects contribute to localized leakage in PSC devices, thereby increasing charge recombination, and reducing both photovoltaic performance and open-circuit voltage [21]. Doping with Cs^+ in $Cs_{0.1}FA_{0.9}PbI_3$ significantly increase in grain size and a marked reduction in grain boundaries. However, the presence of cracks at the grain boundaries may still lead to non-radiative recombination of charge carriers [22]. Doping with Sn^{2+} significantly mitigates this issue, as Sn^{2+} improves the lattice structure, minimizing lattice mismatch at grain boundaries and resulting in a more uniform and smoother film surface [23].

X-ray photoelectron spectroscopy (XPS) analysis (Fig. S1 in the ESM and Figs. 2(e)–2(h)) provides further insights into the

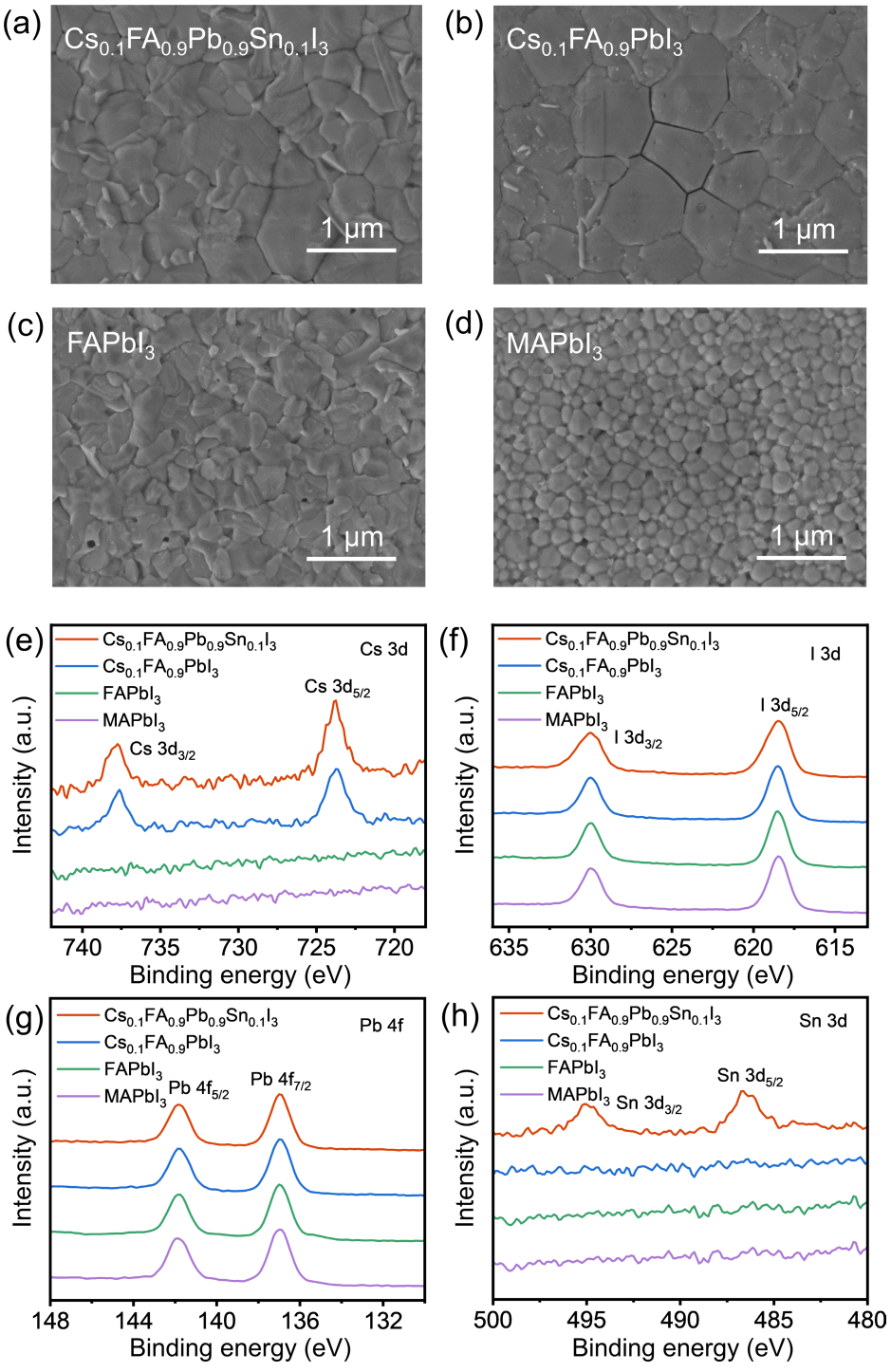

Figure 2 SEM images of the surface morphologies of (a) $Cs_{0.1}FA_{0.9}Pb_{0.9}Sn_{0.1}I_3$, (b) $Cs_{0.1}FA_{0.9}PbI_3$, (c) $FAPbI_3$, and (d) $MAPbI_3$ perovskite films, respectively. High-resolution XPS spectra at (e) Cs 3d, (f) I 3d, (g) Pb 4f, and (h) Sn 3d regions of $MAPbI_3$, $FAPbI_3$, $Cs_{0.1}FA_{0.9}PbI_3$, and $Cs_{0.1}FA_{0.9}Pb_{0.9}Sn_{0.1}I_3$ perovskite films, respectively.

elemental compositions and chemical states of these perovskite materials. The XPS survey spectra in Fig. S1(a) in the ESM identify the element peak positions, while high-resolution XPS spectra for C 1s, N 1s, S 2p, Cs 3d, I 3d, Pb 4f, and Sn 3d regions are compared in Figs. S1(b)–S1(d) in the ESM and Figs. 2(e)–2(h) with calibration based on C 1s at 284.6 eV. Notably, S 2p peaks at 163.5 and 162.0 eV are detected only in the FASCN powder (Fig. S1(d) in the ESM), suggesting that sulfur detaches from the PbI_2 coordination lattice and exits the film as HSCN gas after protonation. Figure 2(e) shows that the peaks at 737.5 and 724.0 eV, corresponding to Cs 3d band, are observed exclusively in $Cs_{0.1}FA_{0.9}PbI_3$ and $Cs_{0.1}FA_{0.9}Pb_{0.9}Sn_{0.1}I_3$ samples, confirming the presence of Cs in these films. Similarly, Sn 3d peaks at 495.0 and 487.0 eV appear solely in the $Cs_{0.1}FA_{0.9}Pb_{0.9}Sn_{0.1}I_3$ sample, indicating successful Sn doping (Fig. 2(h)). XPS binding energies of various elements measured from the as-prepared various perovskite films and FASCN powder are listed in Table S1 in the ESM.

Figures 3(a) and 3(b) illustrates the ultraviolet–visible (UV–Vis)

absorption spectra and corresponding Tauc plots for $MAPbI_3$, $FAPbI_3$, $Cs_{0.1}FA_{0.9}PbI_3$, and $Cs_{0.1}FA_{0.9}Pb_{0.9}Sn_{0.1}I_3$ perovskite films. As shown in Fig. 3(a), $MAPbI_3$ exhibits an absorption edge near 780 nm, while $FAPbI_3$ shows a red shift to approximately 800 nm. The incorporation of Cs^+ into $Cs_{0.1}FA_{0.9}PbI_3$ induces a blue shift to around 795 nm, consistent with the established trend where an increased A-site ion radius leads to a wider tolerance factor and a narrower bandgap [24]. Substituting Pb^{2+} with Sn^{2+} further shifts the absorption edge to 830 nm, signifying a reduction in the bandgap. Variations in absorption intensity across the visible region are observed, with $Cs_{0.1}FA_{0.9}Pb_{0.9}Sn_{0.1}I_3$ exhibiting the highest absorption, followed by $Cs_{0.1}FA_{0.9}PbI_3$, $FAPbI_3$, and $MAPbI_3$. To accurately determine the bandgaps, Tauc plots were constructed (Fig. 3(b)), with the bandgap extracted from the x-intercept of the tangent to the $(Ahv)^2$ versus hv plot [25]. The calculated bandgaps are 1.59 eV for $MAPbI_3$, 1.54 eV for $FAPbI_3$, 1.55 eV for $Cs_{0.1}FA_{0.9}PbI_3$, and 1.50 eV for $Cs_{0.1}FA_{0.9}Pb_{0.9}Sn_{0.1}I_3$, respectively, providing valuable insights into their electronic band structures.

The steady-state photoluminescence (PL) spectra of four perovskite films, excited at a wavelength of 450 nm, are presented in Fig. 3(c). The PL peak positions for $MAPbI_3$, $FAPbI_3$, $Cs_{0.1}FA_{0.9}PbI_3$, and $Cs_{0.1}FA_{0.9}Pb_{0.9}Sn_{0.1}I_3$ are located at 782, 800, 792, and 827 nm, respectively. The observed red or blue shifts align with the trends in their UV–Vis absorption spectra. In terms of PL intensity, the order is $Cs_{0.1}FA_{0.9}Pb_{0.9}Sn_{0.1}I_3$ > $Cs_{0.1}FA_{0.9}PbI_3$ > $FAPbI_3$ > $MAPbI_3$. Interestingly, despite comparable UV–Vis absorption, $Cs_{0.1}FA_{0.9}PbI_3$ exhibits significantly higher PL intensity than $FAPbI_3$, likely due to higher concentration of PbI_2 in $FAPbI_3$, which may convert absorbed energy into internal energy rather than fluorescence [24]. The charge recombination dynamics in perovskite films were further studied through time-resolved photoluminescence (TRPL) spectra, as shown in Fig. 3(d). The scatter plots were fitted using the following biexponential decay equation [16, 20]

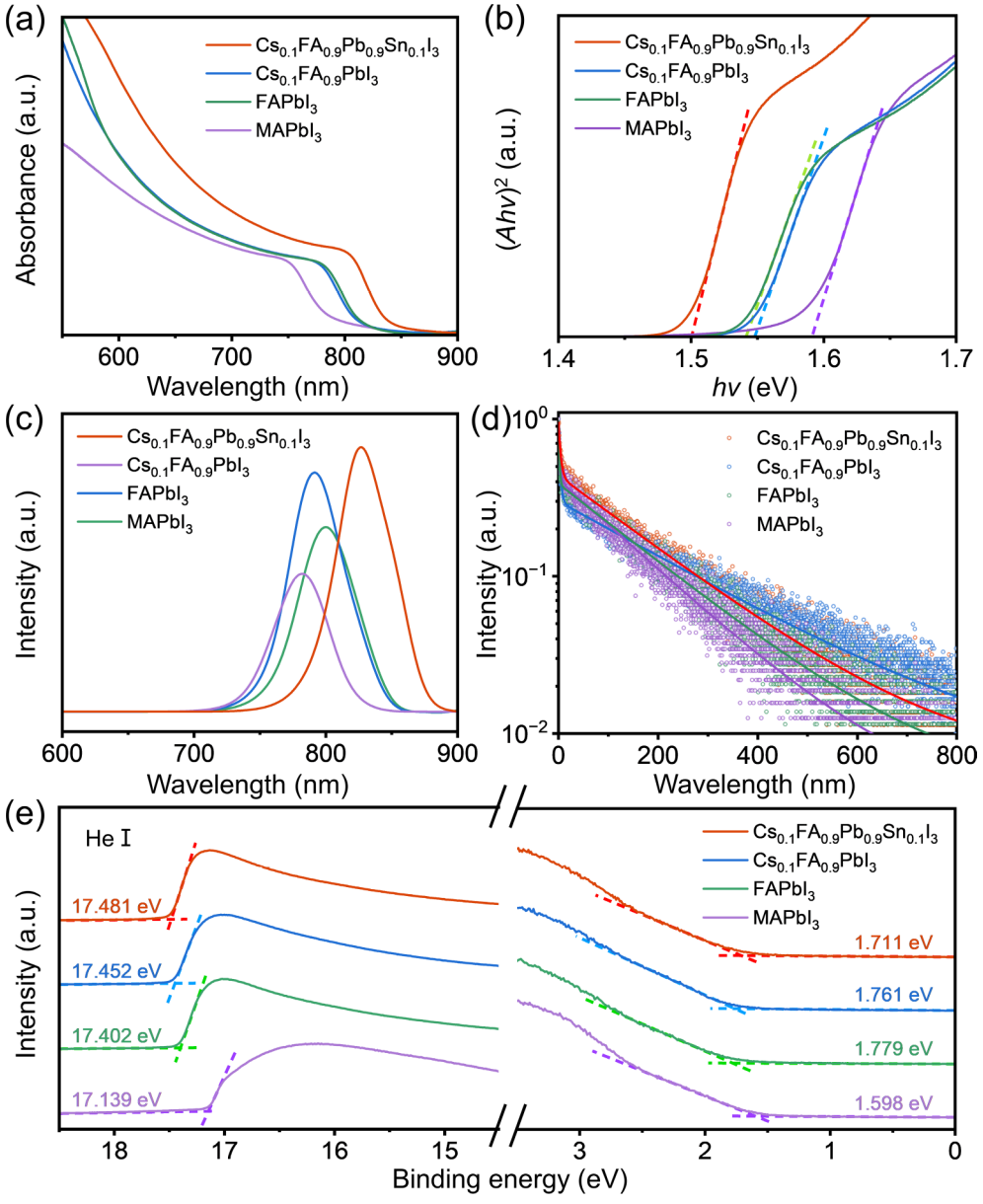

Figure 3 (a) UV–Vis absorption spectra, (b) corresponding Tauc plots, (c) PL spectra, (d) TRPL curves, and (e) UPS curves of $MAPbI_3$, $FAPbI_3$, $Cs_{0.1}FA_{0.9}PbI_3$, and $Cs_{0.1}FA_{0.9}Pb_{0.9}Sn_{0.1}I_3$ perovskite films, respectively.

$$y(t) = A_1\exp(-t/\tau_1) + A_2\exp(-t/\tau_2) \quad (1)$$

where A_1 and A_2 are the decay amplitudes, and τ_1 and τ_2 are the decay times corresponding to trap-assisted grain boundary/interface recombination and free carrier radiative recombination, respectively. The average decay time τ_{avg} was further calculated using the following formula

$$\tau_{avg} = A_1\tau_1 + A_2\tau_2 \quad (2)$$

Among these films, $Cs_{0.1}FA_{0.9}Pb_{0.9}Sn_{0.1}I_3$ exhibited the longest τ_{avg} of 168.06 ns, significantly surpassing $Cs_{0.1}FA_{0.9}PbI_3$ (133.16 ns), $FAPbI_3$ (104.69 ns), and $MAPbI_3$ (71.47 ns). This indicates effective suppression of charge recombination through FASCN passivation [10, 13].

To determine the energy band structures of four perovskites, ultraviolet photoelectron spectroscopy (UPS) was conducted using a He I (21.22 eV) excitation source (Fig. 3(e)). The valence band maximum (E_{VBM}) of the perovskite materials is approximately equal to their work function (W_s), which can be calculated using the following equation [26]

$$h\nu - W_s = E_{cutoff} - E_{fermi} \quad (3)$$

where $h\nu$ is the energy of the incident photons (21.22 eV), E_{cutoff} is the kinetic energy at the cutoff edge, and E_{fermi} is the kinetic energy at the Fermi edge. The E_{VBM} values for $MAPbI_3$, $FAPbI_3$, $Cs_{0.1}FA_{0.9}PbI_3$, and $Cs_{0.1}FA_{0.9}Pb_{0.9}Sn_{0.1}I_3$ are determined to be −5.67, −5.60, −5.53, and −5.45 eV, respectively. Using the optical bandgap values obtained from UV–Vis absorption spectra, the conduction band minimum (E_{CBM}) values for the samples are calculated as −4.09, −4.04, −3.98, and −3.95 eV, respectively.

To further investigate the photovoltaic properties of $MAPbI_3$, $FAPbI_3$, $Cs_{0.1}FA_{0.9}PbI_3$, and $Cs_{0.1}FA_{0.9}Pb_{0.9}Sn_{0.1}I_3$ perovskite films fabricated with the aid of the pseudo-halide SCN^-, the PSCs were developed with the ITO/SnO_2/perovskite/Spiro-OMeTAD/Au configuration, leveraging the prior analysis of their energy band structures. Figures 4(a) and 4(b) illustrates the schematic diagram and cross-sectional SEM image of the device architecture. As depicted in Fig. 4(b), the functional layers exhibit uniform distribution with excellent compactness and coverage, with perovskite layer having a thickness of approximately 900 nm. Based on the UV–Vis absorption and UPS analyses, the optical bandgap

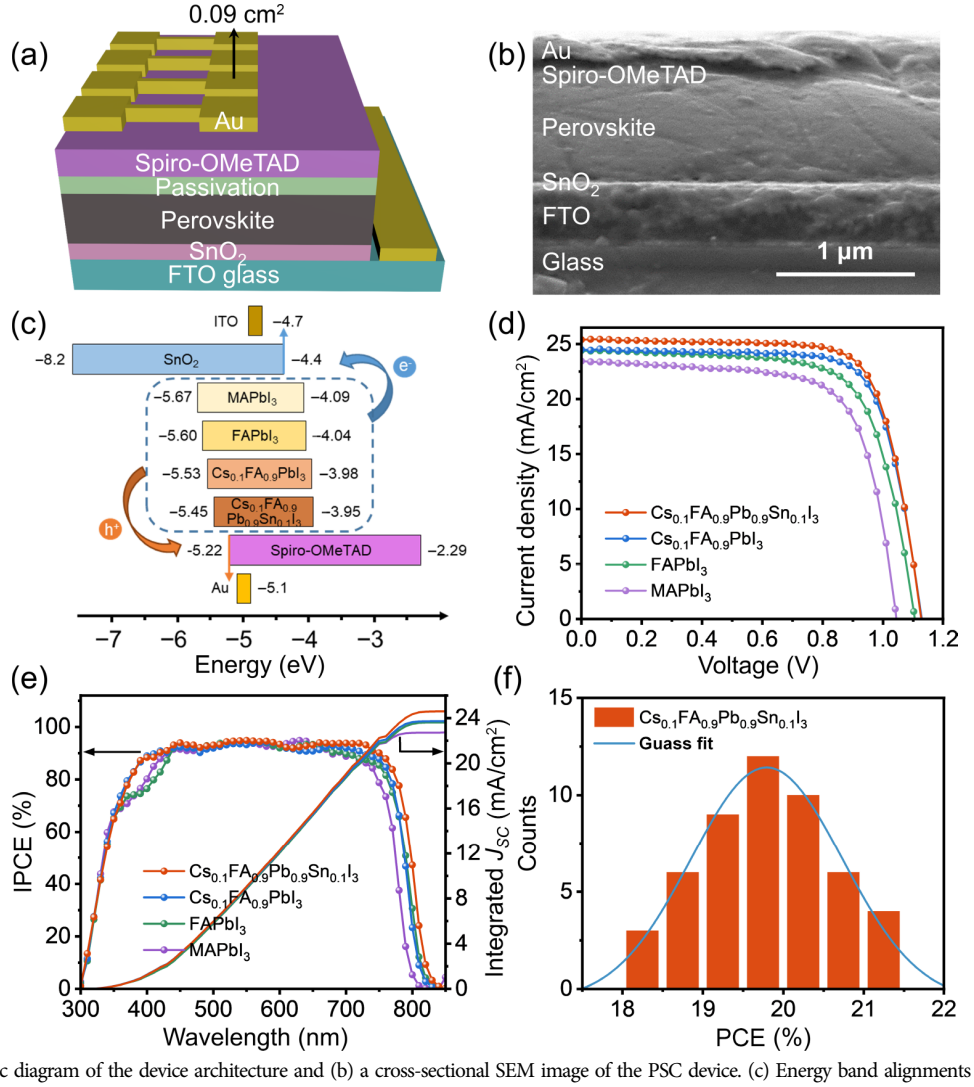

Figure 4 (a) Schematic diagram of the device architecture and (b) a cross-sectional SEM image of the PSC device. (c) Energy band alignments of PSCs with different absorber layers. (d) *J*–*V* curves and (e) IPCE spectra of PSCs based on $MAPbI_3$, $FAPbI_3$, $Cs_{0.1}FA_{0.9}PbI_3$, and $Cs_{0.1}FA_{0.9}Pb_{0.9}Sn_{0.1}I_3$ absorber layers. (f) Statistical histogram of the PCE distribution obtained from 50 individual $Cs_{0.1}FA_{0.9}Pb_{0.9}Sn_{0.1}I_3$ based PSCs.

and the valence band maximum (E_{VBM}) of various absorber layers were determined, as illustrated in Fig. 4(c). These parameters were utilized to derive the overall energy band structure of the device. The favorable energy band alignment, facilitates efficient migration of electrons and holes within the perovskite absorber layer toward the SnO_2 electron transport layer and the Spiro-OMeTAD hole transport layer, respectively, before being collected at the FTO and Au electrodes, and generating current flow through the external circuit [27].

The current density–voltage (J–V) characteristics for the PSCs incorporating $Cs_{0.1}FA_{0.9}Pb_{0.9}Sn_{0.1}I_3$, $Cs_{0.1}FA_{0.9}PbI_3$, $FAPbI_3$ and $MAPbI_3$ absorber layers are illustrated in Fig. 4(d). Key photovoltaic parameters, including open-circuit voltage (V_{OC}), short-circuit current density (J_{SC}), fill factor (FF), and PCE, along with the corresponding optical bandgap values, are summarized in Table S2 in the ESM. Among the tested devices, the $Cs_{0.1}FA_{0.9}Pb_{0.9}Sn_{0.1}I_3$ based PSC demonstrated the highest performance, achieving a V_{OC} of 1.127 V, J_{SC} of 25.399 mA/cm^2, FF of 74.562%, and PCE of 21.343%. This superior performance is attributed to optimal energy band alignment and favorable film morphology. The SCN^- addition together with Cs^+/Sn^{2+} doping markedly narrows the bandgap of $Cs_{0.1}FA_{0.9}Pb_{0.9}Sn_{0.1}I_3$, resulting in a red-shifted optical absorption edge and enhanced light absorption capability in a long-wavelength region (600–800 nm), implying enhanced photon-to-carrier conversion. Concurrently, the SCN^- addition optimizes crystallinity, reduces grain boundary defects and carrier recombination losses, and improves carrier transport efficiency, ultimately leading to enhanced J_{SC} in the devices. In contrast, the $Cs_{0.1}FA_{0.9}PbI_3$ based PSC also exhibits strong efficiency, achieving a V_{OC} of 1.128 V, J_{SC} of 24.497 mA/cm^2, FF of 74.391%, and PCE of 20.556%. Its broader bandgap does not yield a significant advantage in V_{OC}, likely due to suboptimal film morphology. The $FAPbI_3$ based PSC shows a respectable performance with a V_{OC} of 1.105 V, J_{SC} of 24.411 mA/cm^2, FF of 70.187%, and PCE of 18.932%. Although its performance is commendable, it falls short compared to the top-performing devices due to less favorable material properties. Finally, the $MAPbI_3$ based PSC exhibits the lowest performance among the tested samples. The smaller grain size in the film contributes to increased non-radiative recombination centers, while numerous pinholes cause significant leakage [28]. As a result, this device achieves a V_{OC} of 1.045 V, J_{SC} of 23.456 mA/cm^2, FF of 69.872%, and PCE of 17.127%. Photovoltaic parameters of $Cs_{0.1}FA_{0.9}Pb_{0.9}Sn_{0.1}I_3$ based PSCs with different concentrations of FASCN additive are summarized in Table S3 in the ESM. In summary, these results underscore the critical influences of material compositions, crystal structures, and film morphologies on the photovoltaic performance of PSCs.

Figure 4(e) presents the incident photon-to-current conversion efficiency (IPCE) results for the PSCs. The integrated current densities for the $Cs_{0.1}FA_{0.9}Pb_{0.9}Sn_{0.1}I_3$, $Cs_{0.1}FA_{0.9}PbI_3$, $FAPbI_3$, and $MAPbI_3$ devices are 24.58, 23.73, 23.69, and 22.72 mA/cm^2, respectively, closely matching the J_{SC} values in Table S2 in the ESM [29]. All IPCE spectra exhibited a consistent onset at approximately 810 nm (~ 1% IPCE) and high quantum yields (> 80%) in the wavelength range of 380 to 750 nm. To evaluate the reproducibility of the PCE value, 50 individual PSCs based on $Cs_{0.1}FA_{0.9}Pb_{0.9}Sn_{0.1}I_3$ were fabricated. As illustrated in the histogram in Fig. 4(f), the mean PCE was 18.92%, with narrow distribution between 17%–20.5%, underscoring the uniformity and reliability of the fabrication process.

A larger contact angle indicates better hydrophobicity, which can help to prevent water from penetrating into the perovskite layer and causing structural damage [30]. The hydrophobic properties of perovskite films were evaluated through water contact angle measurements on $Cs_{0.1}FA_{0.9}Pb_{0.9}Sn_{0.1}I_3$, $Cs_{0.1}FA_{0.9}PbI_3$, $FAPbI_3$ and $MAPbI_3$ films, as illustrated in Fig. 5(a). Among these, the $Cs_{0.1}FA_{0.9}Pb_{0.9}Sn_{0.1}I_3$ film exhibited the highest contact angle of 64.5°, which is attributed to its superior surface smoothness and gloss. The $Cs_{0.1}FA_{0.9}PbI_3$ film also demonstrated a notable contact angle of 63.7°. In contrast, the $FAPbI_3$ film displayed a lower contact angle of 54.3°, likely due to reduced surface smoothness and lattice density. Although the $MAPbI_3$ film exhibited inferior surface smoothness, it still achieved a contact angle of 58.9°, which can be ascribed to the inherently hydrophobic nature of the material, surpassing that of the FA-based perovskites [30].

The long-term thermal stability of the PSCs based on $Cs_{0.1}FA_{0.9}Pb_{0.9}Sn_{0.1}I_3$, $Cs_{0.1}FA_{0.9}PbI_3$, $FAPbI_3$ and $MAPbI_3$ was investigated under controlled conditions in a nitrogen atmosphere at 25 °C (room temperature) and 85 °C. Figure 5(b) shows the time-dependent variations in PCE at room temperature. Under these conditions, the devices based on $Cs_{0.1}FA_{0.9}PbI_3$ and $Cs_{0.1}FA_{0.9}Pb_{0.9}Sn_{0.1}I_3$ retained 89.57% and 91.65% of their initial PCE values, respectively, after 1000 h. In contrast, the $FAPbI_3$ devices, characterized by substantial bulk PbI_2 residues, experienced lattice strain leading to δ phase decomposition [6], exhibited a substantial decline in PCE to 59.66% after 264 h. The $MAPbI_3$ devices, with smaller grain sizes, exhibited more pronounced lattice collapse, culminating in a PCE of 55.83% after the same duration. Figure 5(c) depicts the thermal stability of these devices under continuous heating at 85 °C. The incorporation of Cs^+ ions significantly enhanced the thermal stability of $Cs_{0.1}FA_{0.9}PbI_3$ and $Cs_{0.1}FA_{0.9}Pb_{0.9}Sn_{0.1}I_3$-based devices, which retained 79.09% and 83.19% of their initial PCE values, respectively, even after 660 h. Conversely, $FAPbI_3$ based device showed a rapid degradation, with the PCE declining to less than 50% of its initial value within 132 h. $MAPbI_3$ based device exhibited a rapid decline to 52.13% of its initial PCE after only 60 h, primarily due to the volatility of the smaller organic MA^+ cations under prolonged thermal stress. These results underscore the critical role of material compositions and structural modulation in determining the thermal resistivity performance of PSCs (Table S4 in the ESM) [11, 30–33].

3 Conclusions

In summary, we successfully fabricated high-quality $Cs_{0.1}FA_{0.9}Pb_{0.9}Sn_{0.1}I_3$ perovskite films by incorporating thiocyanate (SCN^-) as a crystallization facilitator in a two-step spin-coating method. Spectroscopic characterizations revealed that the formation of a reactive intermediate, $PbI_2{\cdot}SCN^-$, which is subsequently displaced by FAI, releasing HSCN gas through proton transfer and volatilization. Comprehensive compositional and structural analyses confirmed the critical role of SCN^- in improving film quality. Notably, the $Cs_{0.1}FA_{0.9}Pb_{0.9}Sn_{0.1}I_3$ sample exhibited optimal surface morphology and interface characteristics, resulting in superior device performance. The PSCs based on $Cs_{0.1}FA_{0.9}Pb_{0.9}Sn_{0.1}I_3$ absorber layers achieved an impressive PCE of 21.34%. Furthermore, these devices demonstrated excellent thermal stability, retaining over 90% of their initial efficiency after 1000 h of operation at 85 °C, highlighting their excellent robustness and potential for practical applications. This study underscores the efficacy of SCN^- in enhancing perovskite film quality and stability,

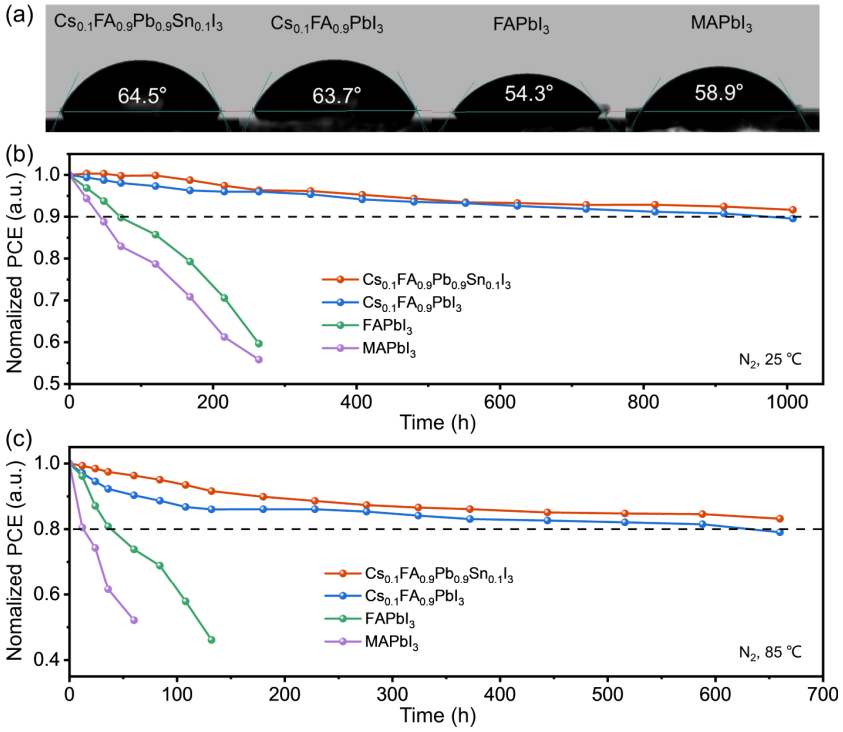

Figure 5 (a) Water contact angle measurements of $Cs_{0.1}FA_{0.9}Pb_{0.9}Sn_{0.1}I_3$, $Cs_{0.1}FA_{0.9}PbI_3$, $FAPbI_3$ and $MAPbI_3$ perovskite films. Long-term operation stability tests under an inert N_2 environment at (b) room temperature (25 °C) and (c) elevated temperature (85 °C, under continuous heating).

while emphasizing the exceptional photovoltaic performance and thermal tolerance of $Cs_{0.1}FA_{0.9}Pb_{0.9}Sn_{0.1}I_3$-based solar cells.

Electronic Supplementary Material: Supplementary Material (Experimental section and additional figures and tables, including XPS spectra, photovoltaic performance parameters, Figs. S1 and S2, and Tables S1–S4) is available in the online version of this article at https://doi.org/10.26599/NR.2025.94907845.

Data availability

All data needed to support the conclusions in the paper are presented in the manuscript and the Electronic Supplementary Material. Additional data related to this paper may be requested from the corresponding author upon request.

Acknowledgements

The authors appreciate the financial support from the National Natural Science Foundation of China (Nos. 22479074 and 22475096), the General Project of the Joint Fund of Equipment Pre-research and the Ministry of Education (No. 8091B02052407), the Natural Science Foundation of Jiangsu Province (Nos. BK20240400 and BK20241236), the Science and Technology Major Project of Jiangsu Province (No. BG2024013), the Scientific and Technological Achievements Transformation Special Fund of Jiangsu Province (No. BA2023037), the Academic Degree and Postgraduate Education Reform Project of Jiangsu Province (No. JGKT24_C001), the Key Core Technology Open Competition Project of Suzhou City (No. SYG2024122), the open research fund of Suzhou Laboratory (No. SZLAB-1308-2024-TS005), the Gusu Leading Talent Program of Scientific and Technological Innovation and Entrepreneurship of Wujiang District in Suzhou City (No. ZXL2021273), and the Chenzhou National Sustainable Development Agenda Innovation Demonstration Zone Provincial Special Project (No. 2023sfq11).

Declaration of competing interest

All the contributing authors report no conflict of interests in this work.

Author contribution statement

Z. J., L. N. Q., and M. F. Z. conceived the idea of this study. L. N. Q. and M. F. Z. performed the preparation of materials. L. N. Q., M. F. Z., and Y. R. X. performed the XRD, FTIR, NMR, and XPS analyses. D. C. H., Y. X. T., H. P. S., and Z. X. T. conducted the photoelectrochemical measurements. Z. J., Y. R. X., L. N. Q., and M. F. Z. analyzed the data and wrote the paper. Z. J., Z. X. T., Y. X., and H. P. S. revised the manuscript and supervised the project. All authors discussed the results and commented on the manuscript.

Use of AI statement

None.

References

[1] Yang, W. S.; Park, B. W.; Jung, E. H.; Jeon, N. J.; Kim, Y. C.; Lee, D. U.; Shin, S. S.; Seo, J.; Kim, E. K.; Noh, J. H. et al. Iodide management in formamidinium-lead-halide-based perovskite layers for efficient solar cells. *Science* **2017**, *356*, 1376–1379.

[2] Kim, N. K.; Min, Y. H.; Noh, S.; Cho, E.; Jeong, G.; Joo, M.; Ahn, S. W.; Lee, J. S.; Kim, S.; Ihm, K. et al. Investigation of thermally induced degradation in $CH_3NH_3PbI_3$ perovskite solar cells using *in-situ* synchrotron radiation analysis. *Sci. Rep.* **2017**, *7*, 4645.

[3] Wang, Z.; Shi, Z. J.; Li, T. T.; Chen, Y. H.; Huang, W. Stability of

perovskite solar cells: A prospective on the substitution of the a cation and X anion. *Angew. Chem., Int. Ed.* **2017**, *56*, 1190–1212.
[4] Wang, S. Y.; Tan, L. G.; Zhou, J. J.; Li, M. H.; Zhao, X.; Li, H.; Tress, W.; Ding, L. M.; Graetzel, M.; Yi, C. Y. Over 24% efficient MA-free $Cs_xFA_{1-x}PbX_3$ perovskite solar cells. *Joule* **2022**, *6*, 1344–1356.
[5] Yi, C. Y.; Luo, J. S.; Meloni, S.; Boziki, A.; Ashari-Astani, N.; Grätzel, C.; Zakeeruddin, S. M.; Röthlisberger, U.; Grätzel, M. Entropic stabilization of mixed A-cation ABX_3 metal halide perovskites for high performance perovskite solar cells. *Energy Environ. Sci.* **2016**, *9*, 656–662.
[6] Zhang, D. D.; Eaton, S. W.; Yu, Y.; Dou, L. T.; Yang, P. D. Solution-phase synthesis of cesium lead halide perovskite nanowires. *J. Am. Chem. Soc.* **2015**, *137*, 9230–9233.
[7] Bu, T. L.; Li, J.; Li, H. Y.; Tian, C. C.; Su, J.; Tong, G. Q.; Ono, L. K.; Wang, C.; Lin, Z. P.; Chai, N. Y. et al. Lead halide-templated crystallization of methylamine-free perovskite for efficient photovoltaic modules. *Science* **2021**, *372*, 1327–1332.
[8] Deng, Y. Y.; Ren, G. H.; Han, D. N.; Han, W. B.; Li, Z. W.; Liu, C. Y.; Guo, W. B. Recent advances in Pb–Sn mixed perovskite solar cells. *J. Energy Chem.* **2022**, *73*, 615–638.
[9] Liang, J.; Zhao, P. Y.; Wang, C. X.; Wang, Y. R.; Hu, Y.; Zhu, G. Y.; Ma, L. B.; Liu, J.; Jin, Z. $CsPb_{0.9}Sn_{0.1}IBr_2$ based all-inorganic perovskite solar cells with exceptional efficiency and stability. *J. Am. Chem. Soc.* **2017**, *139*, 14009–14012.
[10] Senanayak, S. P.; Dey, K.; Shivanna, R.; Li, W. W.; Ghosh, D.; Zhang, Y. C.; Roose, B.; Zelewski, S. J.; Andaji-Garmaroudi, Z.; Wood, W. et al. Charge transport in mixed metal halide perovskite semiconductors. *Nat. Mater.* **2023**, *22*, 216–224.
[11] Tai, Q. D.; You, P.; Sang, H. Q.; Liu, Z. K.; Hu, C. L.; Chan, H. L. W.; Yan, F. Efficient and stable perovskite solar cells prepared in ambient air irrespective of the humidity. *Nat. Commun.* **2016**, *7*, 11105.
[12] Kim, D.; Jung, H. J.; Park, I. J.; Larson, B. W.; Dunfield, S. P.; Xiao, C. X.; Kim, J.; Tong, J. H.; Boonmongkolras, P.; Ji, S. G. et al. Efficient, stable silicon tandem cells enabled by anion-engineered wide-bandgap perovskites. *Science* **2020**, *368*, 155–160.
[13] Lu, H. Z.; Liu, Y. H.; Ahlawat, P.; Mishra, A.; Tress, W. R.; Eickemeyer, F. T.; Yang, Y. G.; Fu, F.; Wang, Z. W.; Avalos, C. E. et al. Vapor-assisted deposition of highly efficient, stable black-phase $FAPbI_3$ perovskite solar cells. *Science* **2020**, *370*, eabb8985.
[14] Jiang, Q.; Zhao, Y.; Zhang, X. W.; Yang, X. L.; Chen, Y.; Chu, Z. M.; Ye, Q. F.; Li, X. X.; Yin, Z. G.; You, J. B. Surface passivation of perovskite film for efficient solar cells. *Nat. Photonics* **2019**, *13*, 460–466.
[15] Zai, H. C.; Su, J.; Zhu, C.; Chen, Y. H.; Ma, Y.; Zhang, P. X.; Ma, S.; Zhang, X.; Xie, H. P.; Fan, R. D. et al. Sandwiched electrode buffer for efficient and stable perovskite solar cells with dual back surface fields. *Joule* **2021**, *5*, 2148–2163.
[16] Zhang, H.; Wu, Y. Z.; Shen, C.; Li, E. P.; Yan, C. X.; Zhang, W. W.; Tian, H.; Han, L. Y.; Zhu, W. H. Efficient and stable chemical passivation on perovskite surface via bidentate anchoring. *Adv. Energy Mater.* **2019**, *9*, 1803573.
[17] Avigad, E.; Etgar, L. Studying the effect of MoO_3 in hole-conductor-free perovskite solar cells. *ACS Energy Lett.* **2018**, *3*, 2240–2245.
[18] Liao, C. H.; Chen, C. H.; Bing, J. M.; Bailey, C.; Lin, Y. T.; Pandit, T. M.; Granados, L.; Zheng, J. H.; Tang, S.; Lin, B. H. et al. Inorganic-cation pseudohalide 2D $Cs_2Pb(SCN)_2Br_2$ perovskite single crystal. *Adv. Mater.* **2022**, *34*, 2104782.
[19] Zhou, Y. Y.; Garces, H. F.; Padture, N. P. Challenges in the ambient Raman spectroscopy characterization of methylammonium lead triiodide perovskite thin films. *Front. Optoelectron.* **2016**, *9*, 81–86.
[20] Wang, F.; Yu, H.; Xu, H. H.; Zhao, N. $HPbI_3$: A new precursor compound for highly efficient solution-processed perovskite solar cells. *Adv. Funct. Mater.* **2015**, *25*, 1120–1126.
[21] Liang, J.; Wang, C. X.; Wang, Y. R.; Xu, Z. R.; Lu, Z. P.; Ma, Y.; Zhu, H. F.; Hu, Y.; Xiao, C. C.; Yi, X. et al. All-inorganic perovskite solar cells. *J. Am. Chem. Soc.* **2016**, *138*, 15829–15832.
[22] Xia, Y. R.; Zhao, C.; Zhao, P. Y.; Mao, L. Y.; Ding, Y. C.; Hong, D. C.; Tian, Y. X.; Yan, W. S.; Jin, Z. Pseudohalide substitution and potassium doping in $FA_{0.98}K_{0.02}Pb(SCN)_2I$ for high-stability hole-conductor-free perovskite solar cells. *J. Power Sources* **2021**, *494*, 229781.
[23] Lian, X. M.; Chen, J. H.; Zhang, Y. Z.; Qin, M. C.; Li, J.; Tian, S. X.; Yang, W. T.; Lu, X. H.; Wu, G.; Chen, H. Z. Highly efficient Sn/Pb binary perovskite solar cell via precursor engineering: A two-step fabrication process. *Adv. Funct. Mater.* **2019**, *29*, 1807024.
[24] Wang, Z. Y.; Zhu, X. J.; Zuo, S. N.; Chen, M.; Zhang, C.; Wang, C. Y.; Ren, X. D.; Yang, Z.; Liu, Z. K.; Xu, X. X. et al. 27%-Efficiency four-terminal perovskite/silicon tandem solar cells by sandwiched gold nanomesh. *Adv. Funct. Mater.* **2020**, *30*, 1908298.
[25] Wang, H. H.; Wang, Z. W.; Yang, Z.; Xu, Y. Z.; Ding, Y.; Tan, L. G.; Yi, C. Y.; Zhang, Z.; Meng, K.; Chen, G. et al. Ligand-modulated excess PbI_2 nanosheets for highly efficient and stable perovskite solar cells. *Adv. Mater.* **2020**, *32*, 2000865.
[26] Xia, Y. R.; Zhu, M. F.; Qin, L. N.; Zhao, C.; Hong, D. C.; Tian, Y. X.; Yan, W. S.; Jin, Z. Organic–inorganic hybrid quasi-2D perovskites incorporated with fluorinated additives for efficient and stable four-terminal tandem solar cells. *Energy Mater.* **2023**, *3*, 300004.
[27] Tumen-Ulzii, G.; Qin, C. J.; Klotz, D.; Leyden, M. R.; Wang, P. P.; Auffray, M.; Fujihara, T.; Matsushima, T.; Lee, J. W.; Lee, S. J. et al. Detrimental effect of unreacted PbI_2 on the long-term stability of perovskite solar cells. *Adv. Mater.* **2020**, *32*, 1905035.
[28] Zhu, M. F.; Qin, L. N.; Xia, Y. R.; Liang, J. C.; Wang, Y. D.; Hong, D. C.; Tian, Y. X.; Tie, Z. X.; Jin, Z. Antimony doped $CsPbI_2Br$ for high-stability all-inorganic perovskite solar cells. *Nano Res.* **2024**, *17*, 1508–1515.
[29] Luo. J.; Yang, L.; Tan, Z.; Xie, W.; Sun, Q.; Li, J.; Du, P.; Xiao, Q.; Wang, L.; Zhao, X. et al. Efficient blue light emitting diodes based on europium halide perovskites. *Adv. Mater.* **2021**, *33*, 2101903.
[30] Xie, Y. M.; Xu, X. W.; Ma, C. Q.; Li, M. L.; Ma, Y. H.; Lee, C. S.; Tsang, S. W. Synergistic effect of pseudo-halide thiocyanate anion and cesium cation on realizing high-performance pinhole-free MA-based wide-band gap perovskites. *ACS Appl. Mater. Interfaces* **2019**, *11*, 25909–25916.
[31] Wang, F.; Jiang, X. Y.; Chen, H.; Shang, Y. Q.; Liu, H. F.; Wei, J. L.; Zhou, W. J.; He, H. L.; Liu, W. M.; Ning, Z. J. 2D-Quasi-2D-3D hierarchy structure for tin perovskite solar cells with enhanced efficiency and stability. *Joule* **2018**, *2*, 2732–2743.
[32] Pious, J. K.; Zwirner, Y.; Lai, H. G.; Olthof, S.; Jeangros, Q.; Gilshtein, E.; Kothandaraman, R. K.; Artuk, K.; Wechsler, P.; Chen, C. et al. Revealing the role of tin fluoride additive in narrow bandgap Pb–Sn perovskites for highly efficient flexible all-perovskite tandem cells. *ACS Appl. Mater. Interfaces* **2023**, *15*, 10150–10157.
[33] Li, Y. Z.; Zhang, Z. B.; Zhou, Y.; Xie, L.; Gao, N. T.; Lu, X. B.; Gao, X. S.; Gao, J. W.; Shui, L. L.; Wu, S. J. et al. Enhanced performance and stability of ambient-processed $CH_3NH_3PbI_{3-x}(SCN)_x$ planar perovskite solar cells by introducing ammonium salts. *Appl. Surf. Sci.* **2020**, *513*, 145790.